



# Characterization of Alloy 709 Commercial Heats

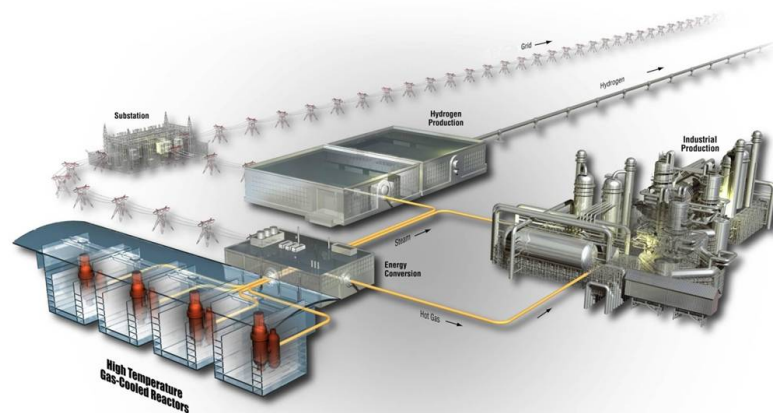
September 2021

Rongjie Song

Caleb D. Clement

Michael D. McMurtrey

*Changing the World's Energy Future*



#### **DISCLAIMER**

This information was prepared as an account of work sponsored by an agency of the U.S. Government. Neither the U.S. Government nor any agency thereof, nor any of their employees, makes any warranty, expressed or implied, or assumes any legal liability or responsibility for the accuracy, completeness, or usefulness, of any information, apparatus, product, or process disclosed, or represents that its use would not infringe privately owned rights. References herein to any specific commercial product, process, or service by trade name, trade mark, manufacturer, or otherwise, does not necessarily constitute or imply its endorsement, recommendation, or favoring by the U.S. Government or any agency thereof. The views and opinions of authors expressed herein do not necessarily state or reflect those of the U.S. Government or any agency thereof.

# **Characterization of Alloy 709 Commercial Heats**

**Rongjie Song**

**Caleb D. Clement**

**Michael D. McMurtrey**

**September 2021**

**Idaho National Laboratory  
Advanced Reactor Technologies  
Idaho Falls, Idaho 83415**

**<http://www.atr.inl.gov>**

**Prepared for the  
U.S. Department of Energy  
Office of Nuclear Energy  
Under DOE Idaho Operations Office  
Contract DE-AC07-05ID14517**

*Page intentionally left blank*



**INLART Program**

**Characterization of Alloy 709 Commercial Heats**

INL EXT-21-64284  
Revision 0

September 2021

Technical Reviewer: (Confirmation of mathematical accuracy, and correctness of data and appropriateness of assumptions.)

  
\_\_\_\_\_  
Ryan Rupp  
ART Materials Engineer

9/1/2021

\_\_\_\_\_  
Date


Approved by:

TING-LEUNG  
SHAM (Affiliate)

Digitally signed by TING-LEUNG  
SHAM (Affiliate)  
Date: 2021.09.01 10:00:38  
-06'00'

\_\_\_\_\_  
T.-L. Sham  
ART Advanced Materials Technical Area Lead

\_\_\_\_\_  
Date



\_\_\_\_\_  
Michael Davenport  
INL ART Project Manager

9/1/2021

\_\_\_\_\_  
Date



\_\_\_\_\_  
Michelle T. Sharp  
INL Quality Assurance

9/1/2021

\_\_\_\_\_  
Date

*Page intentionally left blank*

## ABSTRACT

The creep-resistant austenitic stainless steel Alloy 709 (Fe-20Cr-25Ni (wt%) based steel) is being investigated as a candidate structural material for the next generation of advanced reactors. Unlike conventional solid solution strengthened austenitic stainless steels, Alloy 709 develops a variety of precipitates during aging at different temperatures and times. In this study, precipitate evolution during short-term aging at 775°C was characterized. The effect of aging time (e.g., 10 vs. 100 hours) and cooling after aging (e.g., water quench vs. air cool) on grain size and precipitates have been investigated using light optical microscopy (OM), electron backscatter diffraction (EBSD), transmission electron microscopy (TEM), and energy-dispersive X-ray spectroscopy (EDS).

MX (Ni,Tb)(C,N) and  $M_{23}C_6$  (Cr,Mo)C precipitates were observed in all the statically-aged samples. The grain size distribution in the sample aged for 10 hours and water quenched (10Q) versus the one aged for 100 hours and air cooled (100A) were comparable. This indicates that grain structure was fairly stable when aging at 775°C for up to 100 hours. In contrast, the sample aged for 10 hours and air cooled (10A) showed the smallest and the most uniform grain size distribution. This phenomenon was observed in only one sample. More studies on duplicate samples are needed to confirm the results obtained.

The cooling medium (e.g., water quench vs. air cool) was not observed to impact the size nor the distribution of the MX and  $M_{23}C_6$  precipitates. Increasing the aging time resulted in the following: (1) a decrease in dislocations as well as the number density of small precipitates; (2) an increase in the ratio of free precipitates that were not pinning dislocations; (3) relatively higher N, Nb, and Ti concentration in MX precipitate; (4) some increase in length of  $M_{23}C_6$  carbides which were located on the coherent boundaries; and (5) the introduction of Si-enriched  $M_6X$  precipitates.

The tensile tests at room temperature showed similar properties for each of the static aging treatments, indicating that the differences observed in the microstructural analysis did not have a significant impact on the tensile properties.

*Page intentionally left blank*

## **ACKNOWLEDGEMENTS**

This research was sponsored by the U.S. Department of Energy (DOE), under Contract No. DE-AC07-051D14517 with Idaho National Laboratory (INL), managed and operated by Battelle Energy Alliance (BEA). Programmatic direction was provided by the Office of Nuclear Reactor Deployment of the DOE Office of Nuclear Energy.

The authors gratefully acknowledge the support provided by Sue Lesica, Federal Lead for Advanced Materials, Advanced Reactor Technologies (ART) Program; Brian Robinson, Federal Manager, ART Fast Reactors (FR) Campaign; and Robert Hill of Argonne National Laboratory (ANL), National Technical Director, ART FR Campaign.

The authors would like to acknowledge the other Alloy 709 development and code case testing team members for helpful discussions: Ryann Rupp, Ting-Leung Sham, and Richard Wright from INL, Xuan Zhang from ANL, and George Young from Kairos Power. The authors deeply appreciate the technical support provided by Yaqiao Wu, Sheng Cheng, Yu Lu, and Megha Dubey from Boise State University Center for Advanced Energy Studies (CAES). The authors also deeply appreciate the assistance with sample preparation provided by Tom Lillo, Rick Hatch, Wesley Jones, and Bryan Forsmann from INL.

*Page intentionally left blank*

# CONTENTS

ABSTRACT.....	v
ACKNOWLEDGEMENTS.....	vii
ACRONYMS.....	xiii
1. INTRODUCTION.....	1
2. EXPERIMENTAL PROCEDURE .....	2
2.1 Material .....	2
2.1.1 Material Produced by Electralloy/G. O. Carlson .....	2
2.1.2 Material Produced by ATI .....	2
2.2 Experimental Procedure.....	2
2.2.1 Light Optical Microscopy (LOM).....	2
2.2.2 Electron Backscatter Diffraction (EBSD).....	3
2.2.3 Transmission Electron Microscopy (TEM) .....	3
2.2.4 Tensile Testing.....	4
3. RESULTS AND DISCUSSION .....	5
3.1 Material Produced by Electralloy/G. O. Carlson .....	5
3.1.1 Microstructure Evolution (As-rolled, Solution-Annealed and Static Aging).....	5
3.1.2 Grain Boundary and Twin.....	6
3.1.3 MX Precipitates .....	7
3.1.4 $M_{23}C_6$ .....	8
3.1.5 $M_6X$ ( $\eta$ Carbide) .....	11
3.1.6 Z-phase.....	13
3.1.7 Small Precipitate and Dislocation Density.....	14
3.1.8 Effect of Heat Treatment during Static Aging on Microstructure .....	15
3.1.9 Results of Tensile Testing.....	16
3.2 Material Produced by ATI .....	17
4. CONCLUSIONS.....	17
5. SUGGESTED FUTURE WORK.....	19
6. REFERENCES.....	20

## FIGURES

Figure 1. A schematic showing the five sampling locations across sample thickness for light optical micrography (e.g., S1, Q1, C, Q2, and S2).....	3
Figure 2. Across thickness light optical micrographs of the specimens processed by hot rolling and solution annealing at 1150°C for 60 min followed by water quench [1]......	5
Figure 3. Across thickness light optical micrographs of the specimens processed by hot rolling, solution annealing at 1150°C for 60 min, and static aging at 775°C for different holding times and either water quenched or air cooled. (a-e) sample 10Q; (f-j) sample 10A; and (k-o) sample 100A. Key: surface 1 (S1); quarter 1 (Q1); center (C); quarter 2 (Q2), surface 2 (S2). All images were taken at the same magnification. The red arrow in (i) shows a large inclusion about 500 $\mu\text{m}$ in length.....	6
Figure 4. EBSD images of the static-aged samples 10A (a-d), and 100A (e-h). (a,c,e,g) Inverse pole figure maps with the color code displayed in (g). (b,d,f,h) Image quality maps of high-angle grain boundaries with misorientation angles greater than or equal to 15 degrees indicated by blue lines, low-angle grain boundaries with misorientation angles of less than 5 degrees and 5 to 15 degrees marked by red and green lines, respectively; the grain boundary misorientation legend is shown in (h).....	7
Figure 5. MX precipitate in 10A sample.....	8
Figure 6. MX precipitate in 100A sample.....	8
Figure 7. $\text{M}_{23}\text{C}_6$ at grain boundary in 10Q sample.....	9
Figure 8. Plate shaped $\text{M}_{23}\text{C}_6$ grew initially at incoherent twin boundary in 10Q sample.....	9
Figure 9. $\text{M}_{23}\text{C}_6$ enriched with Cr and Mo formed in the grain interiors in 10A sample.....	9
Figure 10. $\text{M}_{23}\text{C}_6$ nucleated around MX core in 10A sample.....	10
Figure 11. TTT diagram for $\text{M}_{23}\text{C}_6$ in Alloy 709 using Thermo-Calc databases TCFE9 and MOBFE4 [10]......	11
Figure 12. $\text{M}_6\text{X}$ precipitate ( $\eta$ carbide) in 100A sample. (a) Bright field TEM image; (b) selected area diffraction (SAD) pattern of selected area in (a); (c) HAADF-STEM image, the same area as in (a). The shaded area of O1 is enriched Ni and Si, which was formed on the edge of area of O2, a MX precipitate; (d) Bright field STEM image, the same area as in (a); (e) EDS profiles for various elements along the line shown in the image (d). .....	12
Figure 13. Simulated TTP diagram of the 1150°C solution-annealed Alloy 709 for 0.1% transformation.....	13
Figure 14. TEM image of the 100A sample showing the pinning of some of the by Z-phase precipitates (a); and (b) SAD pattern of the selected area in (a).....	14
Figure 15. TEM images of small size precipitates (<50 nm) and dislocations from the sample of (a) 10Q and (b) 100A. The red arrows point at the precipitates “freely floating” in the matrix and the yellow arrows highlight the precipitates pinning dislocations.....	14
Figure 16. Engineering stress-strain curve of the 10Q, 10A and 100A samples. ....	17



## TABLES

Table 1. Chemical composition of the ESR Alloy 709 ingot (wt%), heat #: 58776-1R. ....	2
Table 2. Chemical composition of the Alloy 709 ingot produced by ATI (wt.%) heat # 529900-01, piece ID: CG05455. ....	2
Table 3. M6X ( $\eta$ Carbide) key composition in 100A sample, at%. ....	12
Table 4. Density of small precipitates (<50 nm) and dislocation density in 10Q, 10A and 100A samples. ....	15
Table 5. MX precipitate key composition and size in 10Q, 10A, and 100A samples. ....	15
Table 6. Globular $M_{23}C_6$ key composition and size in 10Q, 10A, and 100A samples. ....	16
Table 7. Plate $M_{23}C_6$ key composition and size in 10Q, 10A, and 100A samples. ....	16

*Page intentionally left blank*

## ACRONYMS

ANL	Argonne National Laboratory
ART	Advanced Reactor Technologies
ASME	American Society of Mechanical Engineers
ASTM	American Society for Testing and Materials
ATI	Allegheny Technologies Incorporated
DOE	U.S. Department of Energy
EBS	electron backscatter diffraction
EDS	energy-dispersive X-ray spectroscopy
ESR	electroslag remelting
FHR	fluoride-salt-cooled high-temperature reactor
FY	fiscal year
HAADF	high-angle annular dark-field
INL	Idaho National Laboratory
LOM	light optical microscopy
ND	normal direction
NRC	U.S. Nuclear Regulatory Commission
OM	optical microscopy
ORNL	Oak Ridge National Laboratory
RD	rolling direction
SAD	selected area diffraction
SEM	scanning electron microscopy
SFR	sodium-cooled fast reactor
STEM	scanning transmission electron microscopy
TD	transverse direction
TEM	transmission electron microscopy
TIA	TEM instrument and analysis
TTP	time-temperature-precipitation
TTT	time-temperature-transformation

*Page intentionally left blank*

# Characterization of Alloy 709 Commercial Heats

## 1. INTRODUCTION

Austenitic stainless steels are employed in many engineering applications, including conventional and nuclear power plants because of their high-temperature strength and corrosion resistance due to their high nickel and chromium content, as well as the economic feasibility of iron-based alloys. Fe-20Cr-25Ni advanced austenitic stainless steel (NF709) was developed by Nippon Steel for boiler tubing applications. A plate form of Alloy 709 was developed for elevated temperature nuclear applications in sodium-cooled fast reactors (SFRs) because of its desired high-temperature mechanical properties [1].

Alloy 709 has a similar chemical composition as NF709 and is intended for SFR applications that include the reactor vessel, core supports, primary and secondary piping, and possibly the intermediate heat exchanger and compact heat exchanger. There is also interest in using Alloy 709 for Fluoride-Salt-Cooled High-Temperature Reactor (FHR) applications.

Because of the significant enhancement in time-dependent mechanical properties of Alloy 709 relative to 316H stainless steel (a reference construction material for SFR systems), code qualification of Alloy 709 was recommended. A comprehensive plan for the development of a 500,000-hour, 760°C American Society of Mechanical Engineers (ASME) code case and the resolution of structural integrity issues identified by the U.S. Nuclear Regulatory Commission (NRC) for Alloy 709 was developed [2]. A staged qualification approach for Alloy 709 was devised. This necessitates the generation of multiple data packages to support multiple code cases with increasing design lives up to 500,000 hours. The first phase of this plan includes a 100,000-hour, 650°C ASME code case, as well as the initiation of very long-term creep tests, thermal-aging studies, and sodium-exposure tests.

A program comprised of U.S. Department of Energy (DOE) national laboratories (e.g., Argonne National Laboratory [ANL], Idaho National Laboratory [INL], and Oak Ridge National Laboratory [ORNL]) and Advanced Reactor Technologies (ART) is in progress to qualify Alloy 709 [2]. This program has resulted in two commercial heats of Alloy 709 plate being procured. The first commercial heat, heat 58776, was fabricated by Electralloy/G. O. Carlson in fiscal year (FY)-2017 [1]. The processing condition that resulted in the best balance of creep and creep-fatigue properties was identified. This was the electroslag remelting (ESR) final processing step, with an 1150°C solution anneal, and age hardened at 775°C for 10 hours followed by air cooling [3]. Data generated from this processing condition will be used to form the data packages for code qualification. The purpose of this age hardening heat treatment is to form beneficial precipitates prior to service. These precipitates form during accelerated testing, but concern does exist regarding whether they would form at the low-temperature, low-stress conditions anticipated during service [4]. This age-hardening heat treatment also improves the creep-fatigue properties without significantly impacting the creep properties [3]. The second commercial heat of Alloy 709 was ordered from Allegheny Technologies Incorporated (ATI) in FY-2020 [5]. Heat 529900 was received March 2021.

The sensitivity of the age-hardening heat treatment needs to be established. Industrial heat treating of large-scale components may not be able to be as stringently controlled as compared to a laboratory setting. Consequently, this report investigates two variations of this age-hardening heat treatment: (1) 775°C for 10 hours and water quenched; and (2) 775°C for 100 hours and air cooled. In addition, this report includes a preliminary characterization of the precipitates present in the ATI heat in the solution-annealed condition.

## 2. EXPERIMENTAL PROCEDURE

### 2.1 Material

#### 2.1.1 Material Produced by Electralloy/G. O. Carlson

A subsection of Alloy 709 commercial heat 58776 was cast to an approximately 12-in. thick and 42-in. wide (305-mm thick x 1067-mm wide) cross-section ingot using ESR by Electralloy/G. O. Carlson. The ESR ingot chemistry is available in Table 1. The slab was reheated and hot-rolled at a starting temperature of 1200°C to a final cross-section of 1.1-in. thick x 60-in. wide (e.g., ~28-mm thick x 1524-mm wide). The hot-rolled plate was subjected to solution anneal by isothermal holding at 1150°C for 60 minutes followed by water quench [1]. Three static aging treatments were then applied on the 1150°C solution-annealed plates: (1) aged at 775°C for 10 hours and water quenched (sample ID: 10Q); (2) aged at 775°C for 10 hours and air cooled (sample ID: 10A); and (3) aged at 775°C for 100 hours and air cooled (sample ID: 100A). The 10Q, 10A, and 100A samples were obtained at the same location in terms of width in the hot-rolled plate and were in the area of roughly 10–30 in. away from the mill edge.

Table 1. Chemical composition of the ESR Alloy 709 ingot (wt%), heat #: 58776-1R.

C	Mn	Si	P	S	Cr	Ni	Mo
0.066	0.9	0.39	0.014	0.001	20.06	25.12	1.50
N	Nb	Ti	Cu	Co	Al	B	Fe
0.16	0.26	0.02	0.06	0.02	0.02	0.0035	Bal <sup>1</sup>

Bal<sup>1</sup> Balance

#### 2.1.2 Material Produced by ATI

Alloy 709 heat 529900 was cast and hot-rolled by ATI. The hot-rolled plate is 1.75 in. (e.g., ~44 mm) thick and was subjected to solution anneal by isothermal holding at 1150 C minimum followed by water quench. Table 2 shows the heat chemistry.

Table 2. Chemical composition of the Alloy 709 ingot produced by ATI (wt.%) heat # 529900-01, piece ID: CG05455.

C	Mn	Si	P	S	Cr	Ni	Mo
0.08	0.9	0.39	0.003	<0.001	19.9	24.6	1.50
N	Nb	Ti	Cu	Co	Al	B	Fe
0.15	0.17	<0.01	0.06	0.02	0.02	0.0040	Bal <sup>1</sup>

Bal<sup>1</sup> Balance

## 2.2 Experimental Procedure

#### 2.2.1 Light Optical Microscopy (LOM)

The static-aged specimens were sectioned and mounted in Bakelite such that the observation area is on the cross-section of the normal direction-transverse direction plane (e.g., normal direction [ND], transverse direction [TD]), and the observation direction was parallel to the rolling direction (RD). The specimens were polished with silicon carbide paper up to 1200 grit size. A subsequent electrolytic etching

was applied with 10% oxalic acid in water at 2.2V and room temperature for 60 s. As shown in Figure 1, the light optical micrographs were taken at five locations across the sample thickness in the normal direction (e.g., S1: surface 1; Q1: quarter 1; C: center; Q2: quarter 2; S2: surface 2).

The post-annealed specimens were sectioned and mounted in Bakelite such that the observation area is on the cross-section of the normal direction-transverse direction plane (e.g., ND, TD), and the observation direction was parallel to the RD. The specimens were polished with silicon carbide paper up to 1200 grit size. A subsequent electrolytic etching was applied with 10% oxalic acid in water at 2.2V and room temperature for 60 s. As shown in Figure 1, the light optical micrographs were taken at five locations across the sample thickness in the normal direction (e.g., S1, Q1, C, Q2, S2).

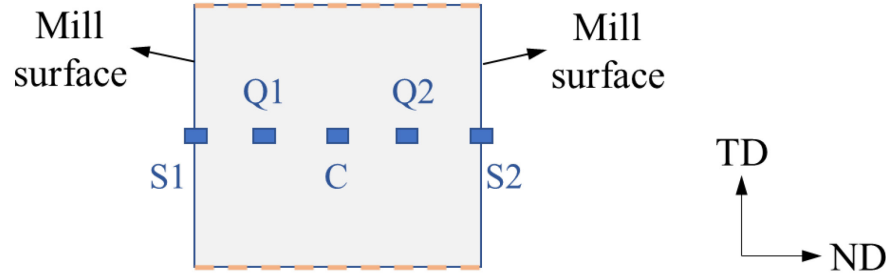


Figure 1. A schematic showing the five sampling locations across sample thickness for light optical micrography (e.g., S1, Q1, C, Q2, and S2).

### 2.2.2 Electron Backscatter Diffraction (EBSD)

For the EBSD sample preparation, after silicon carbide paper polishing to 1200 grit size, the specimens were polished using 3.0- $\mu\text{m}$  and 1.0- $\mu\text{m}$  diamond slurries and were final-polished using a vibratory polisher with a 0.05- $\mu\text{m}$  colloidal silica for 8–12 hours. EBSD measurements were performed on a JEOL JSM-6610LV scanning electron microscopy (SEM) with EBSD. The area of measurement was  $250 \times 250 \mu\text{m}^2$  with a step size of 0.8  $\mu\text{m}$ . TSL OIM software was used to analyze the EBSD data. Grain boundaries with misorientation angles 2 to 15 degrees were considered as low-angle grain boundaries, and boundaries with misorientation angles greater than or equal to 15 degrees were considered as high-angle grain boundaries. Precipitates appear as dark spots in the EBSD map.

### 2.2.3 Transmission Electron Microscopy (TEM)

Samples were prepared for TEM by grinding and polishing until a thickness of approximately 100  $\mu\text{m}$  or less was reached. Close to the quarter thickness area, discs measuring 3 mm in diameter were punched out and subjected to twin jet electropolishing with 10% perchloric acid in ethanol at 15 V and -15 C until perforation. TEM observations were performed using FEI Tecnai F30-FEG with energy-dispersive X-ray spectroscopy (EDS) operating at 300 kV. The TEM observation direction was the same as the light optical microscopy (OM) and was parallel to the RD. Down-zone axis bright field scanning transmission electron microscopy (STEM) imaging was used for dislocation images. Electron diffraction and EDS were used for the phase identification. High-angle annular dark-field (HAADF) imaging in STEM was also used to provide high resolution images.

ImageJ and TIA were used to investigate precipitate size in the samples examined. For the rod-like precipitates, dimensions were acquired by measuring the width and length of the precipitate for each sample. For all other sample morphologies, the longest diameter of the precipitate was measured. The number density of small precipitates was measured by taking a count of the total number of precipitates in each micrograph or area of micrograph, then dividing by the area and an assumed thickness of 100 nm. The dislocation density was measured by taking a count of the total number of dislocations in each micrograph or area of micrograph, then dividing by the area measured.

#### **2.2.4 Tensile Testing**

Tensile testing was performed following American Society for Testing and Materials (ASTM) E8 testing standard practices at room temperature [6]. Each specimen was marked with a standard 25.4 mm gauge length indenter and then measured for initial diameter, initial gauge length marking, and initial v-notch length of the specimen before each test using calibrated calipers. An Instron Dynamic Extensometer Model 2620-824 with a 25.4 mm gauge length was calibrated in accordance with ASTM E83 B-2 criterion using an Epsilon Calibrator Stand Model 3590 and mounted onto the specimen in relation the indented gauge mark section of the specimen. The load frame test control was implemented with Instron Bluehill 3 software using a crosshead speed of 0.5 mm/min to maintain a stress rate between 1.15 and 11.5 MPa/s in accordance with Control Method A of ASTM E8 for determining yield properties. At approximately 19% strain the test was paused, and the Instron Dynamic Extensometer was removed to prevent over extension. The test was then resumed with crosshead displacement as the means of obtaining strain values for the remainder of the test. At test completion the specimen was removed and measured for final diameter, final gauge length marking, and final v-notch length of the specimen. All measurement devices had active calibrations on record in accordance with the INL Standards and Calibrations Laboratory.



### 3. RESULTS AND DISCUSSION

#### 3.1 Material Produced by Electralloy/G. O. Carlson

##### 3.1.1 Microstructure Evolution (As-rolled, Solution-Annealed and Static Aging)

Figure 2 displays the microstructure after solution annealing at 1150 C for 60 min followed by water quench. Figure 3 displays the microstructure after the subsequent static aging (i.e., isothermal holding) at 775°C for: (1) 10 hours and water quench (see Figure 3a-e); (2) 10 hours and air cool (see Figure 3f-j); and (3) 100 hours and air cool (see Figure 3k-o). An inhomogeneous grain size distribution was observed regardless of the difference in heat treatments. In comparison to the effect of heat treatment, the 10A sample shows the smallest and most uniform grain size distribution, while the 10Q and 100A samples both have a higher quantity of abnormal grain growth throughout the normal thickness. However, this does not reflect the effect of cooling rate and is instead likely due to variations within the sample and the location where the grains were imaged. As seen in Figure 2, for example, some areas have quite large grains, as observed from Figure 2(1-3), and some have very fine grain structures, as can be seen from Figure 2(4-7), so depending on the locations imaged within a single specimen, different grain structures could be observed. The black area pointed to by a red arrow in Figure 3i seems to be a large inclusion. However, it is not common that the elongated direction of the inclusion is parallel rather than perpendicular to the normal direction in hot-rolled product. This necessitates a more detailed study since large inclusions can be detrimental to the mechanical behavior of the alloy.

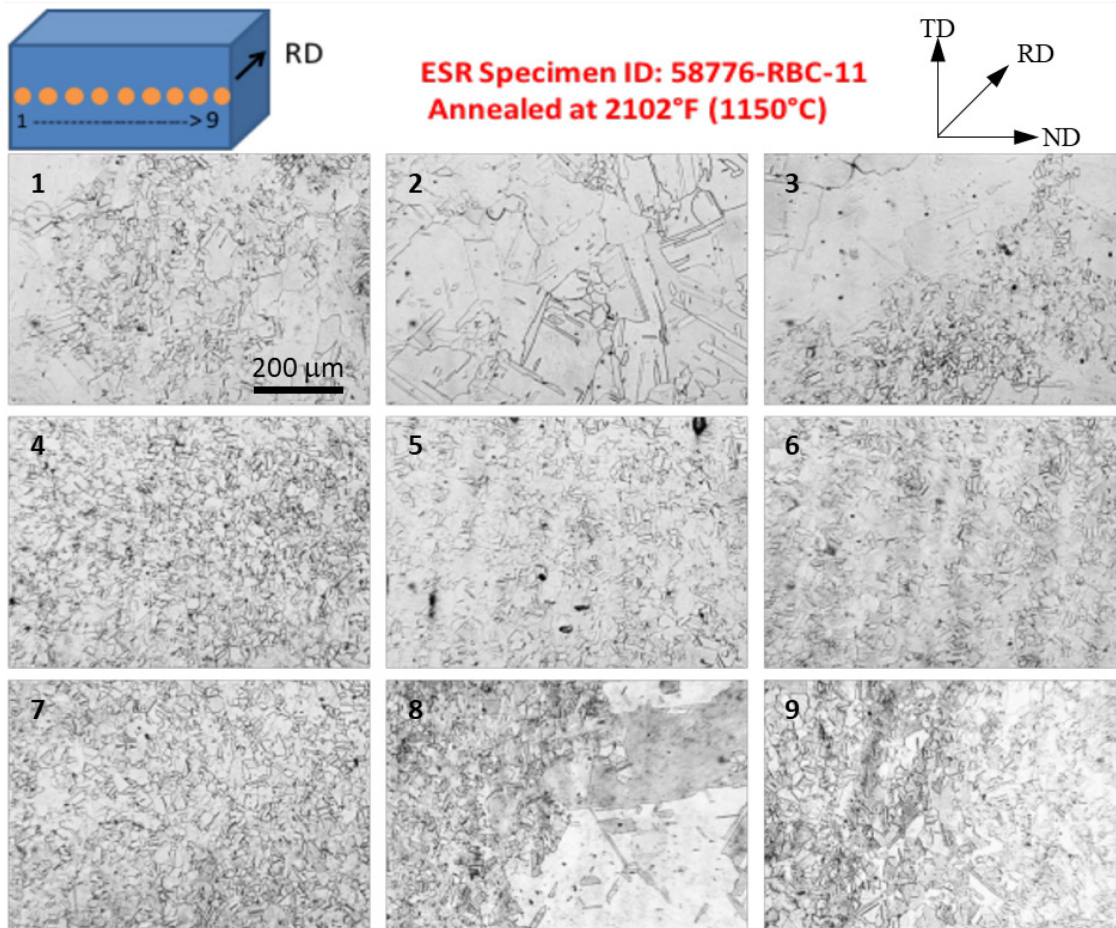


Figure 2. Across thickness light optical micrographs of the specimens processed by hot rolling and solution annealing at 1150°C for 60 min followed by water quench [1].

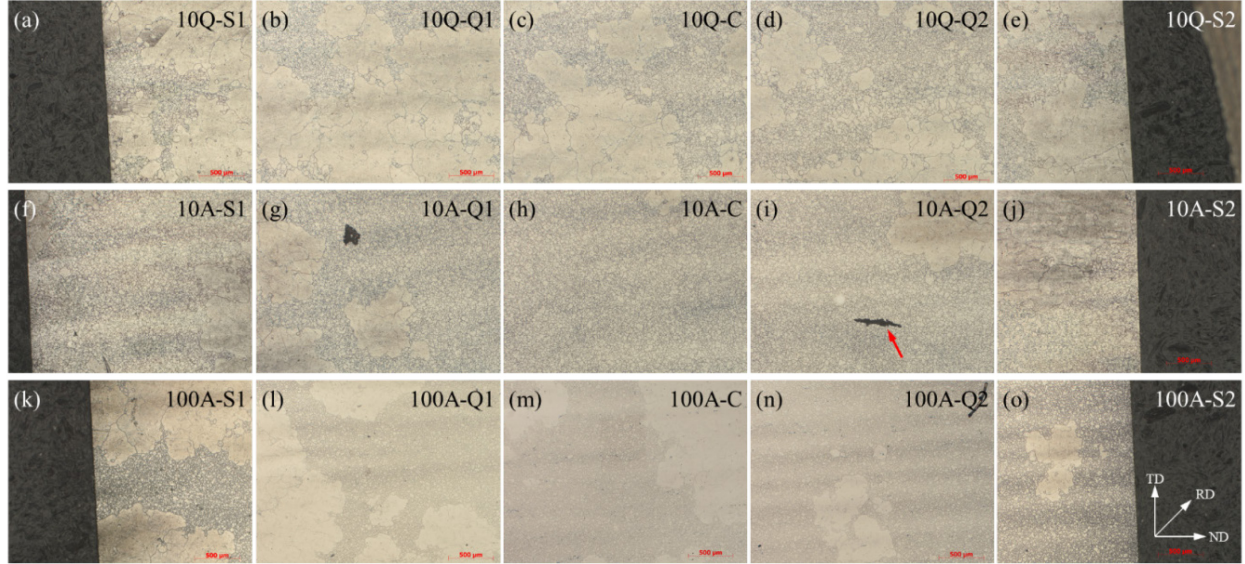


Figure 3. Across thickness light optical micrographs of the specimens processed by hot rolling, solution annealing at 1150°C for 60 min, and static aging at 775°C for different holding times and either water quenched or air cooled. (a-e) sample 10Q; (f-j) sample 10A; and (k-o) sample 100A. Key: surface 1 (S1); quarter 1 (Q1); center (C); quarter 2 (Q2), surface 2 (S2). All images were taken at the same magnification. The red arrow in (i) shows a large inclusion about 500  $\mu\text{m}$  in length.

It is recommended to re-etch and take light OM of the material after solution annealing at 1150°C at the same magnification of 50X. This is the same magnification used for the age-hardened specimen images. Therefore, a direct comparison can be made to confirm there is no unexpected microstructure evolution after static aging at 775°C, such as recovery and/or abnormal grain growth.

### 3.1.2 Grain Boundary and Twin

Figure 4 shows the EBSD images of static-aged samples after isothermal holding at 775°C for 10 hours followed by air cooling (a-d), and for 100 hours followed by air cool (e-h). The areas with small grains are displayed in Figure 4(a,b,e,f), while the areas with both small and large grains are represented in Figure 4(c,d,g,h). The random color distribution in the inverse pole figure maps in figure 4(a,c,e,g) implies there is no evidence of strong texture in the annealed samples, which is as expected. The image quality maps in figure 4(b,d,f,h) show high-angle grain boundaries with misorientation angles greater than or equal to 15 degrees, which were indicated by blue lines, low-angle grain boundaries with misorientation angles of less than 5 degrees and 5 to 15 degrees, which were marked by red and green lines, respectively. It can be seen that most of the boundaries are high-angle grain boundaries and the microstructure consist of a large number of annealing twins. Compared to the 10A sample, the 100A sample had a relatively lower density of annealing twins.



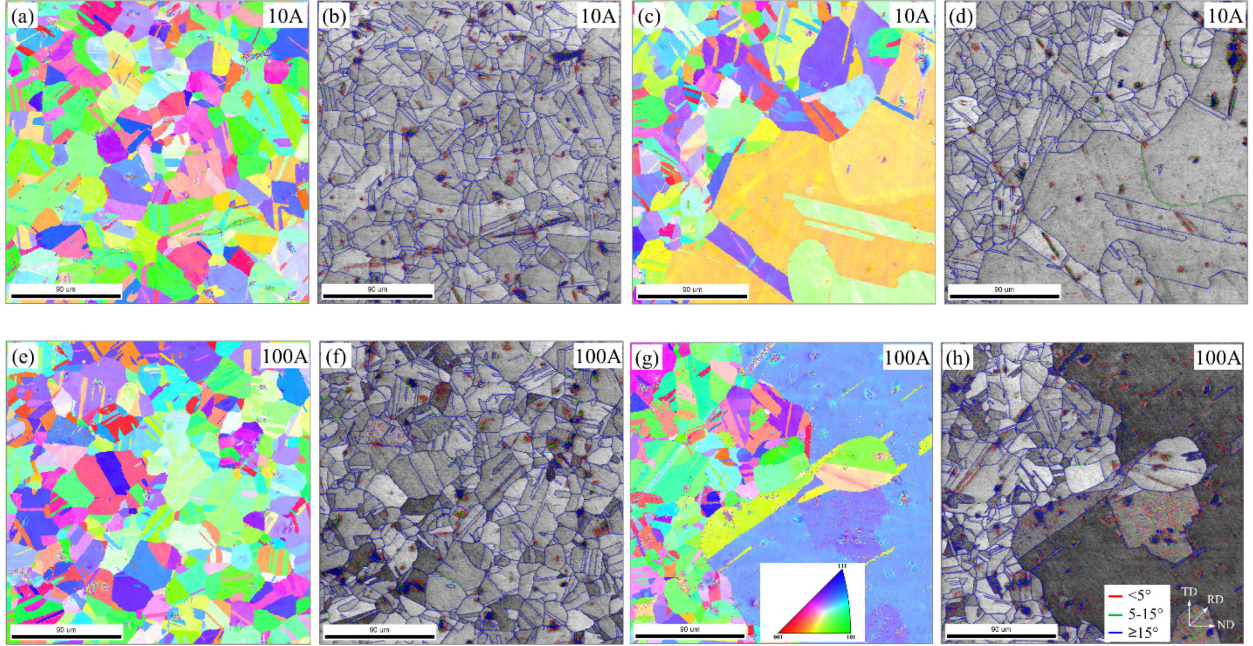


Figure 4. EBSD images of the static-aged samples 10A (a-d), and 100A (e-h). (a,c,e,g) Inverse pole figure maps with the color code displayed in (g). (b,d,f,h) Image quality maps of high-angle grain boundaries with misorientation angles greater than or equal to 15 degrees indicated by blue lines, low-angle grain boundaries with misorientation angles of less than 5 degrees and 5 to 15 degrees marked by red and green lines, respectively; the grain boundary misorientation legend is shown in (h).

### 3.1.3 MX Precipitates

MX precipitates (M is Nb or Ti, X is C or N) can be observed in all static-aged samples (e.g., 10Q, 10A, and 100A). Figure 5 and Figure 6 are the examples of MX precipitates in both 10A and 100A samples. This is consistent with several previous studies [7] that demonstrated the first phase to form during aging was MX in the Fe-25Ni-20Cr steel. Before the static aging, the material was solution-annealed at 1150°C. According to the Irvine equation [8], shown below as Equation (1), approximately 0.018 wt.% Nb precipitates will be dissolved into solution. The subsequent water quench from 1150°C produced a solution supersaturated with C, N, and Nb supersaturation. Consequently, during static aging (e.g., at 775°C), these elements are rejected from solution to form Nb(C,N) or TiNb(C,N). Additionally, the Nb(CN) particles act as nucleation sites for the  $M_{23}C_6$  carbides.

$$T = 6700 / (2.26 - \log[Nb][C + 12/14N]) \quad (1)$$

where:

[x] = the element content in wt%

T is temperature in Kelvin

log = logarithm in base 10.

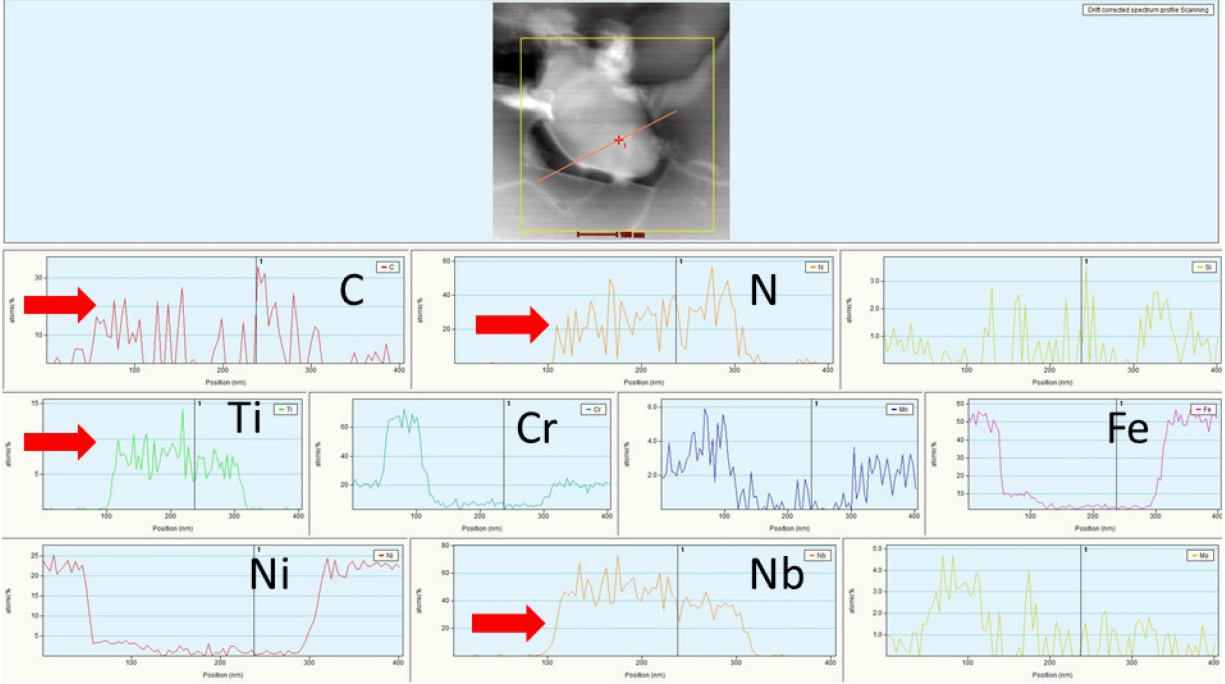


Figure 5. MX precipitate in 10A sample.

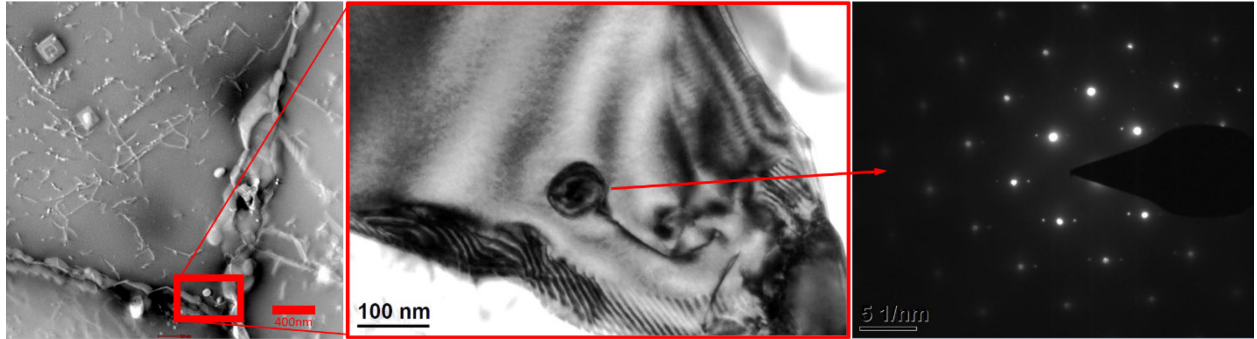


Figure 6. MX precipitate in 100A sample.

### 3.1.4 $M_{23}C_6$

Aging of alloy compositions with stabilization ratios  $[Nb \text{ wt.\%} / (C + N \text{ wt.\%})]$  below 7.7 (stoichiometric composition) should result in the precipitation of  $M_{23}C_6$  ((Cr,Mo)C). In the investigated Alloy 709, the Nb/(C + N) ratio is 1.15; thus,  $M_{23}C_6$  is generally expected.  $M_{23}C_6$  is indeed the most frequently observed precipitate in this study, with a variety of shapes and locations. For instance, globular  $M_{23}C_6$  was observed preferentially at the grain boundaries, as shown in Figure 7, while the plates grew initially at incoherent twin boundaries, as observed in Figure 8. Additionally, block shaped  $M_{23}C_6$  precipitates formed in the grain interiors, as can be seen in Figure 9. As an example, Figure 9 also shows the  $M_{23}C_6$  precipitates enriched with Cr and Mo contents. The blocky  $M_{23}C_6$  precipitates in the grain interior nucleated on MX, shown in Figure 10, or dislocations. Sourmail observed the formation of  $M_{23}C_6$  after very short aging times (e.g., 30 min) at 750°C in a stabilized stainless steel [9]. The time-temperature-transformation (TTT) curve of  $M_{23}C_6$  in Alloy 709, calculated using Thermo-Calc databases TCFE9 and MOBFE4, exhibits a C-shape with a nose temperature of approximately 800°C as shown in Figure 11 [10]. These findings are in accordance with our observations that  $M_{23}C_6$  is the most frequently observed precipitate.



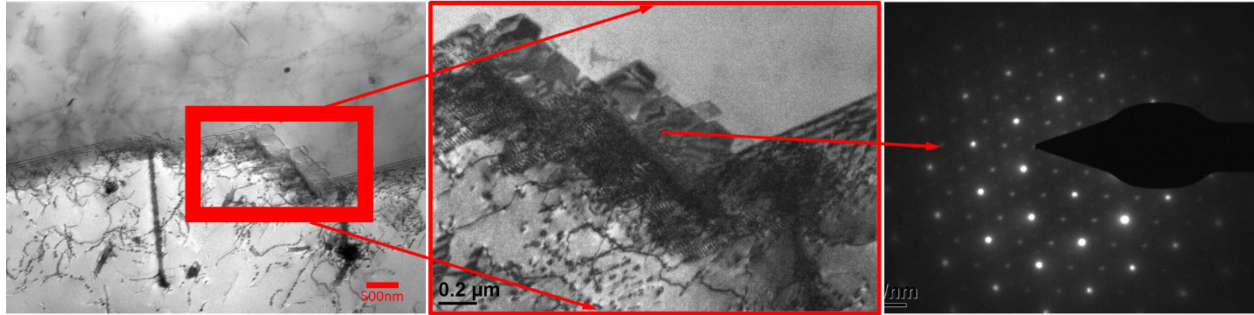


Figure 7.  $M_{23}C_6$  at grain boundary in 10Q sample.

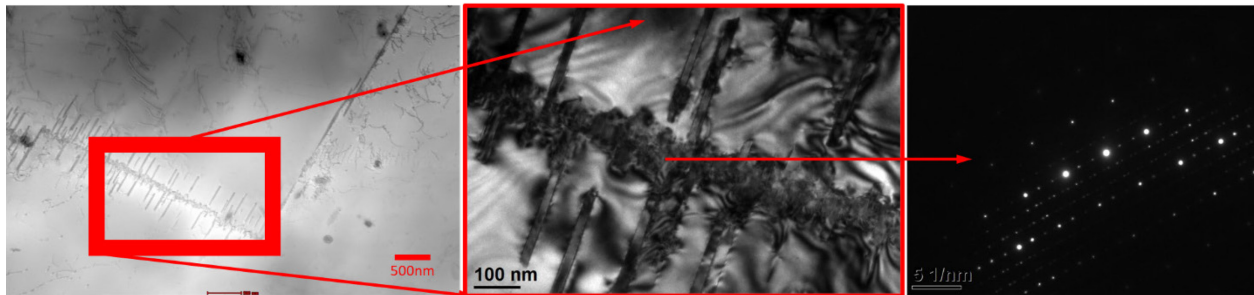


Figure 8. Plate shaped  $M_{23}C_6$  grew initially at incoherent twin boundary in 10Q sample.

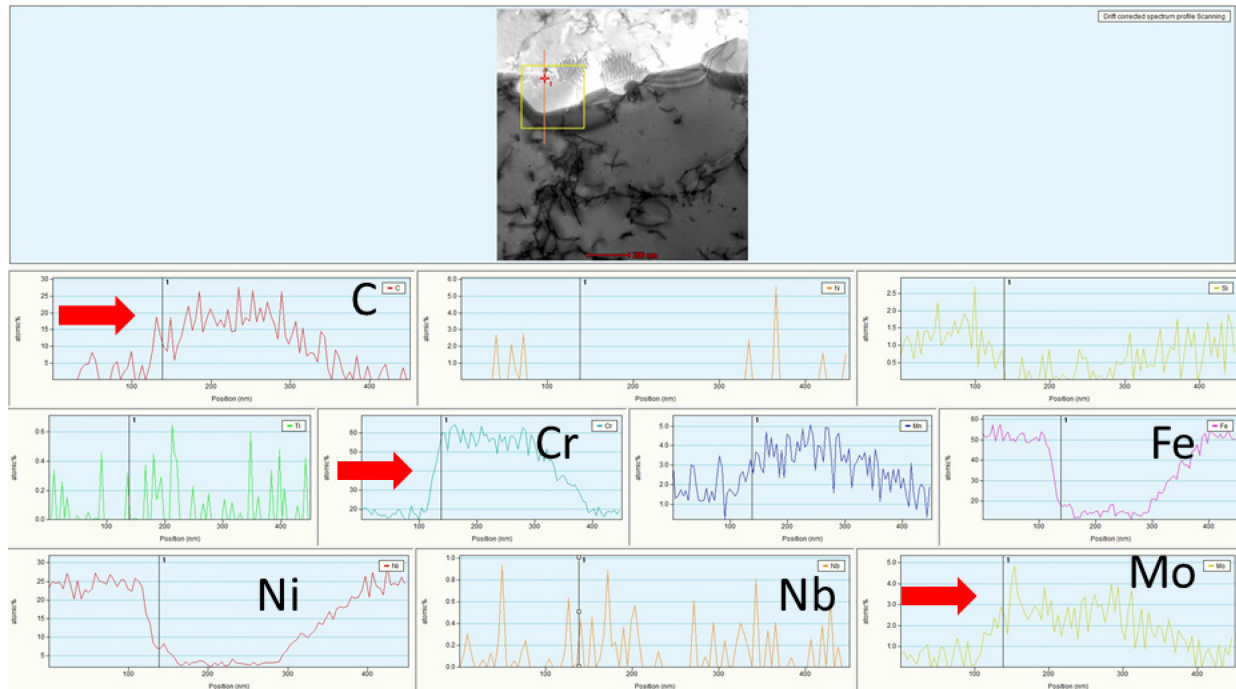


Figure 9.  $M_{23}C_6$  enriched with Cr and Mo formed in the grain interiors in 10A sample.

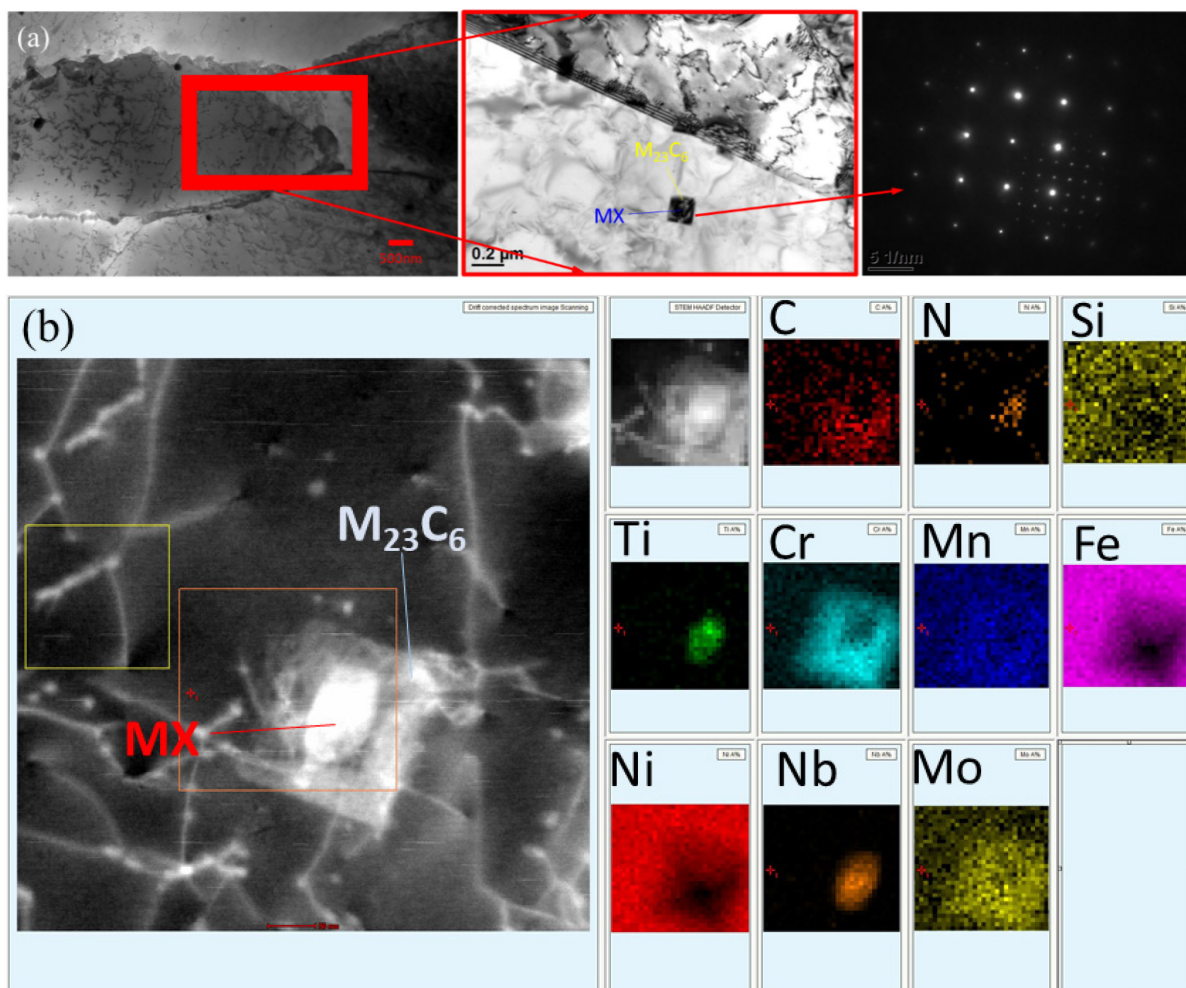


Figure 10.  $\text{M}_{23}\text{C}_6$  nucleated around MX core in 10A sample.

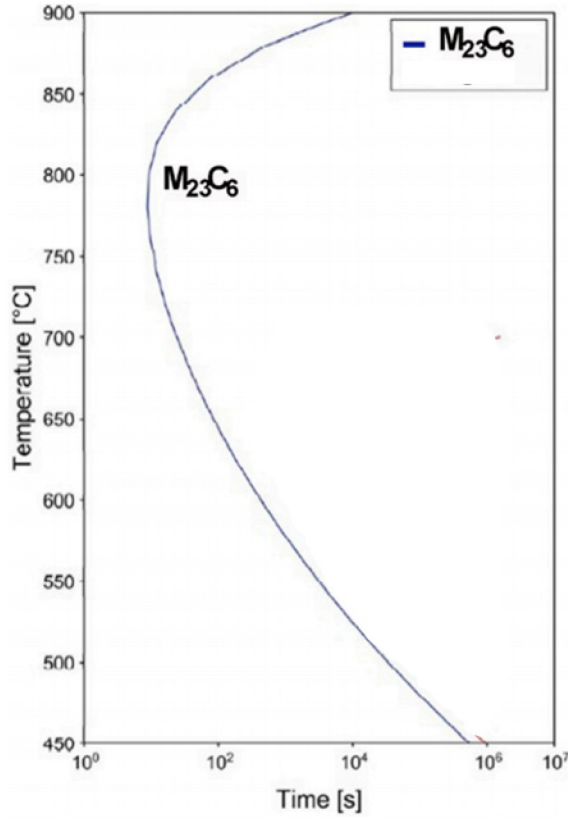


Figure 11. TTT diagram for  $M_{23}C_6$  in Alloy 709 using Thermo-Calc databases TCFE9 and MOBFE4 [10].

### 3.1.5 $M_6X$ ( $\eta$ Carbide)

The  $M_6X$  precipitate  $Cr_3Ni_2SiX$  has a diamond-cubic structure, but it has an extremely similar lattice parameter to  $M_{23}C_6$ , which has a cubic structure.  $M_6X$  was found to occur at similar locations as  $M_{23}C_6$ , and to have a similar morphology, therefore making it difficult to distinguish one from the other without chemical compositional or careful diffraction analysis. Figure 12 displays the TEM images, diffraction pattern, and EDS profile of the  $M_6X$  precipitate in the 100A sample. As shown in the EDS profile along the line in Figure 12e, the shaded area of O1 in Figure 12(c,d) is enriched with Ni and Si, which was formed on the edge of area of O2 with  $M_{23}C_6$  precipitate. This can be attributed to the formation of  $M_{23}C_6$  firstly, then Ni- and Si-enriched on the existing  $M_{23}C_6$ . Table 3 displays the chemical composition of the MX precipitate in 100A sample. In this study,  $M_6X$  precipitate was only observed in the sample after longer aging time of 100 hours. This agrees with the time-temperature-precipitation (TTP) simulation performed using the JMatPro software in Figure 13 (e.g., 0.1% of MX is expected to have precipitated after heat treating at 775°C for 10 hours)<sup>a</sup>.

<sup>a</sup> Zhang, X., G.A. Young, and T.-L. Sham. Private Communication, 2021

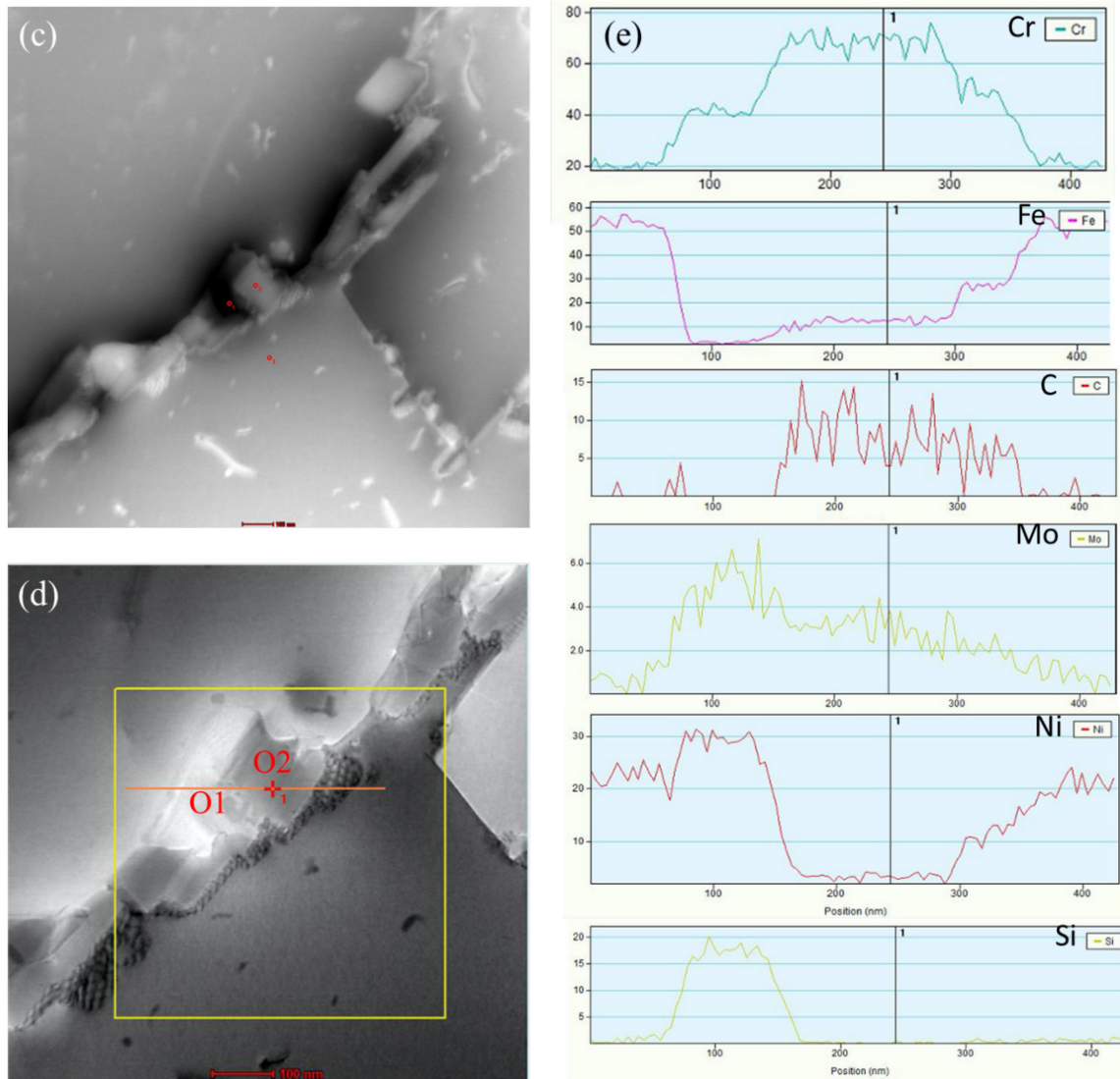
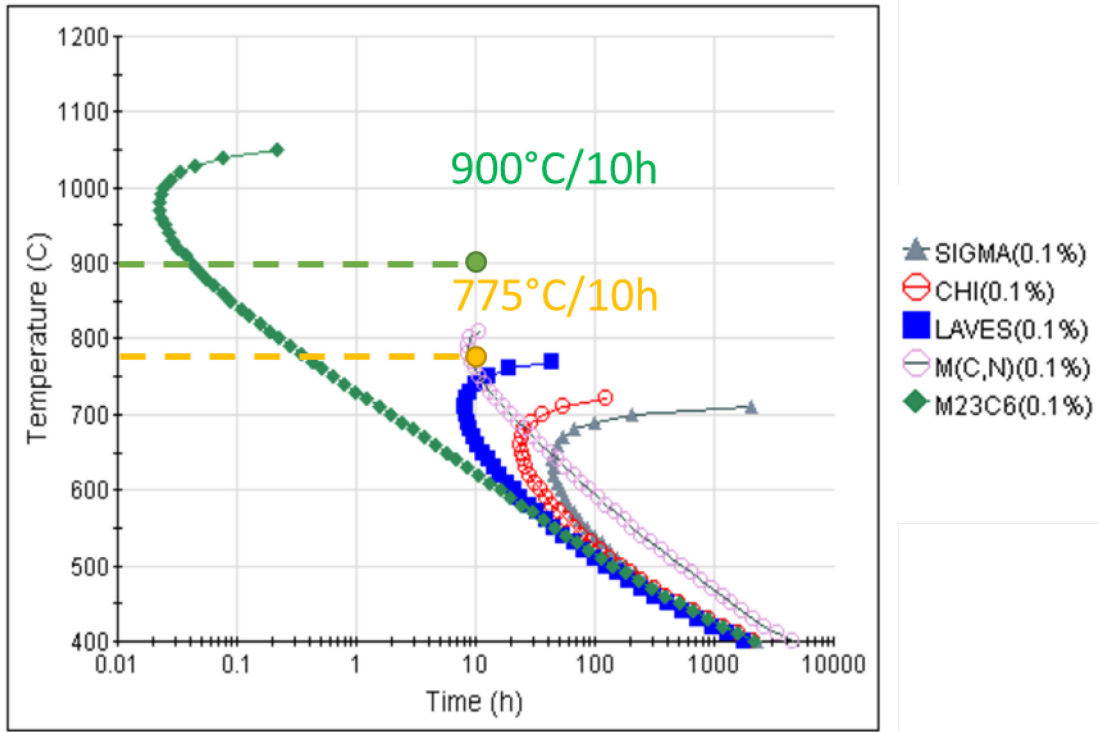


Figure 12.  $M_6X$  precipitate ( $\eta$  carbide) in 100A sample. (a) Bright field TEM image; (b) selected area diffraction (SAD) pattern of selected area in (a); (c) HAADF-STEM image, the same area as in (a). The shaded area of O1 is enriched Ni and Si, which was formed on the edge of area of O2, a MX precipitate; (d) Bright field STEM image, the same area as in (a); (e) EDS profiles for various elements along the line shown in the image (d).

Table 3.  $M_6X$  ( $\eta$  Carbide) key composition in 100A sample, at%.

	C(K)	N(K)	Si(K)	Cr(K)	Fe(K)	Ni(K)	Mo(K)
<b>100A</b>	$0.74 \pm 0.27$	$0.38 \pm 0.13$	$11.00 \pm 0.69$	$37.96 \pm 1.27$	$17.49 \pm 1.80$	$25.53 \pm 0.71$	$3.96 \pm 0.17$





Quench temperature: 1150 °C

Figure 13. Simulated TTP diagram of the 1150°C solution-annealed Alloy 709 for 0.1% transformation.

### 3.1.6 Z-phase

Z-phase is a nitride with the formula  $\text{CrNbN}$ , which usually forms in Nb-stabilized austenitic stainless steels with a high content of nitrogen [9]. It has been reported that Z-phase can form at elevated temperature [11] and is due to conversion of pre-existing NbN precipitates [12]. According to the study of Ding et al. [7] in Alloy 709, Z-phase did not form at 550°C, but started to precipitate during aging at 650°C. The precipitates were nucleated on dislocations and their number increased with aging time and temperature. In this study, the Z-phase was observed in the 100A sample, as shown in Figure 14. The Z-phase and small MX are difficult to deconvolute; further investigation is required.

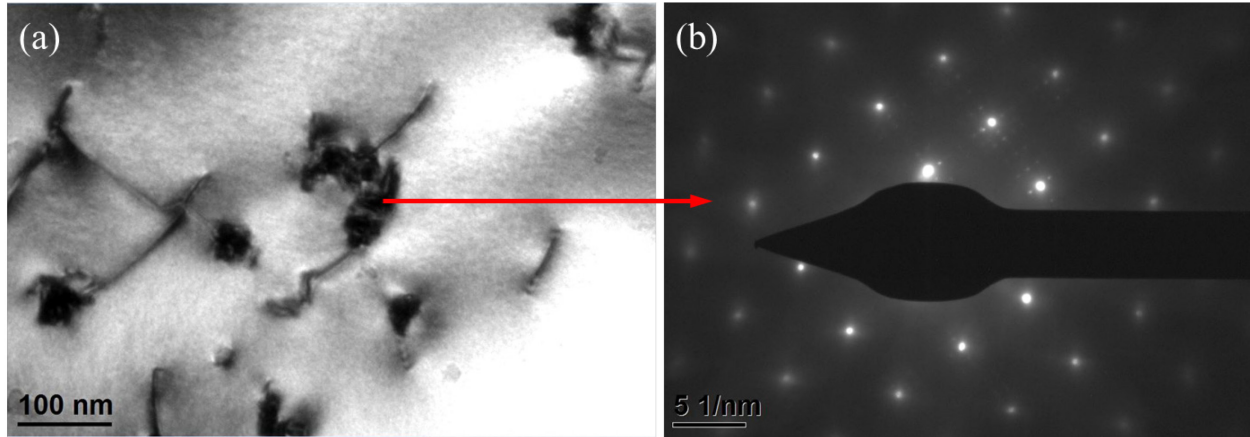


Figure 14. TEM image of the 100A sample showing the pinning of some of the by Z-phase precipitates (a); and (b) SAD pattern of the selected area in (a).

### 3.1.7 Small Precipitate and Dislocation Density

The TEM images in Figure 15 show some small precipitates ( $<50$  nm) in the 10Q (a) and 100A (b) samples. The small precipitates are referred as small MX and Z-phase. They are either “freely floating” in the matrix (pointed by the red arrows) or pinning dislocations (highlighted by the yellow arrows). Table 4 lists the number density of small precipitates and dislocation density in the 10Q, 10A, and 100A samples. In comparison to the 10Q sample, the 10A sample has higher number density of small precipitates and higher dislocation density. The 100 hours aging led to a decrease in both small precipitate and dislocation density, and a higher ratio of free precipitates to total precipitates (including both freely floating and pinning dislocation precipitates) in the 100A sample, as can be observed in Table 4.

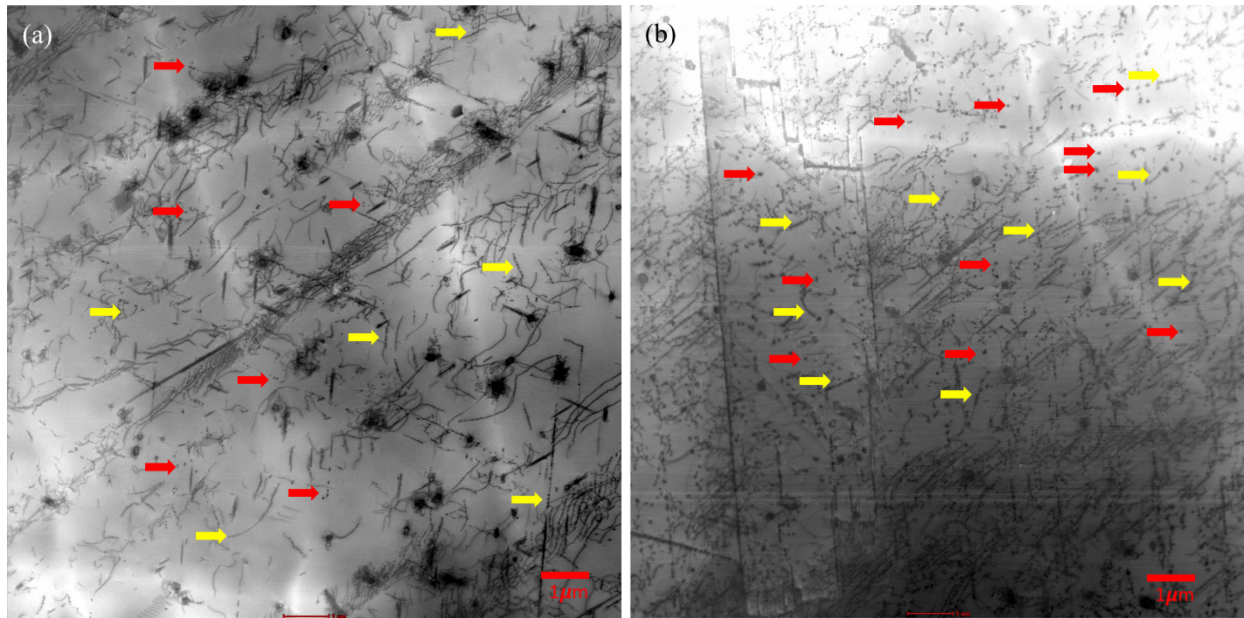


Figure 15. TEM images of small size precipitates ( $<50$  nm) and dislocations from the sample of (a) 10Q and (b) 100A. The red arrows point at the precipitates “freely floating” in the matrix and the yellow arrows highlight the precipitates pinning dislocations.

Table 4. Density of small precipitates (&lt;50 nm) and dislocation density in 10Q, 10A and 100A samples.

Sample	Number Density of Small Precipitate ( $10^{19}\text{m}^{-3}$ )	Ratio of Free Precipitates to Total Precipitates (Free and Pinned)	Dislocation Density ( $10^{12}\text{m}^{-2}$ )
10Q	$8.21 \pm 0.21$	$0.22 \pm 0.01$	$5.03 \pm 0.14$
10A	$26.2 \pm 4.18$	$0.25 \pm 0.01$	$13.2 \pm 1.19$
100A	$18.5 \pm 0.62$	$0.43 \pm 0.4$	$7.51 \pm 0.02$

### 3.1.8 Effect of Heat Treatment during Static Aging on Microstructure

The prominent precipitate in the solution-annealed Alloy 709 is MX (M is Nb or Ti, X is C or N). After static aging at 775°C for 10 hours, in addition to MX precipitates,  $\text{M}_{23}\text{C}_6$  precipitates were also observed in all the investigated samples. This is because  $\text{M}_{23}\text{C}_6$  precipitates can form after very short aging times (e.g., 30 min) at 775°C, as shown in Figure 11. Some of the  $\text{M}_{23}\text{C}_6$  precipitates nucleated around MX precipitates in the 10A sample resulting in an MX core. This implies the formation of  $\text{M}_{23}\text{C}_6$  precipitates is after that of MX precipitates, as observed in Figure 10. In comparison to the 10Q sample, as shown in Tables 5-7, there is no obvious difference in MX and  $\text{M}_{23}\text{C}_6$  precipitates in the 10A sample according to precipitate composition and size. However, comparing to the 10Q sample, the 10A sample has a higher dislocation density and higher number density of small precipitates, as shown in Table 4. The higher dislocation density can be due to the pinning effect resulting from the higher number density of small precipitates in the 10A sample.

Compared to the 10A sample, 100 hours of aging led to a decrease in both small precipitates and dislocation density, as well as a higher ratio of free precipitates to total precipitates (including both freely floating and pinning dislocation precipitates) in the 100A sample, as seen in Table 4. Besides MX and  $\text{M}_{23}\text{C}_6$ , new Si enriched  $\text{M}_6\text{X}$  precipitates were observed in the 100A sample after 100 hours static aging, as observed in Figure 12 and Table 3. In the 100A sample, the MX precipitate consisted of relatively higher N, Nb and Ti composition, shown in Table 5, and longer length of  $\text{M}_{23}\text{C}_6$ , shown in Table 6 and Table 7, which may demonstrate some increase in  $\text{M}_{23}\text{C}_6$  size on the coherent boundaries after 100 hours holding.

Table 5. MX precipitate key composition and size in 10Q, 10A, and 100A samples.

Sample	MX precipitate key composition, at%						MX precipitate size, $\mu\text{m}$	
	C(K)	N(K)	Ti(K)	Fe(K)	Ni(K)	Nb(K)	Matrix	Grain Boundary
10Q	$1.87 \pm 0.85$	$0.39 \pm 0.31$	$2.21 \pm 0.76$	$30.30 \pm 4.57$	$13.63 \pm 2.26$	$23.99 \pm 6.08$	$140 \pm 17$	$140 \pm 28$
10A	$0.58 \pm 0.27$	$3.43 \pm 0.91$	$3.41 \pm 0.91$	$33.21 \pm 2.86$	$15.20 \pm 1.4$	$23.49 \pm 3.78$	$185 \pm 21$	$218 \pm 34$
100A	$2.94 \pm 0.66$	$12.64 \pm 1.39$	$7.06 \pm 0.39$	$10.04 \pm 1.13$	$4.49 \pm 0.53$	$43.21 \pm 1.72$	$200 \pm 44$	$220 \pm 32$

Table 6. Globular  $M_{23}C_6$  key composition and size in 10Q, 10A, and 100A samples.

Sample	Globular $M_{23}C_6$ key composition, at%					Globular $M_{23}C_6$ size, $\mu m$	
	C(K)	Cr(K)	Fe(K)	Ni(K)	Mo(K)	Matrix	Grain Boundary
10Q	4.79 $\pm 0.87$	42.86 $\pm 3.24$	34.66 $\pm 2.42$	14.55 $\pm 1.27$	1.48 $\pm 0.16$	173 $\pm 18$	284 $\pm 26$
10A	6.57 $\pm 2.31$	37.00 $\pm 4.91$	37.49 $\pm 4.61$	15.67 $\pm 2.67$	1.45 $\pm 0.33$	168 $\pm 21$	154 $\pm 28$
100A	7.95 $\pm 3.15$	58.96 $\pm 5.16$	20.94 $\pm 4.74$	8.24 $\pm 2.39$	2.78 $\pm 0.52$	193 $\pm 33$	338 $\pm 84$

Table 7. Plate  $M_{23}C_6$  key composition and size in 10Q, 10A, and 100A samples.

Sample	Plate $M_{23}C_6$ key composition, at%					Plate $M_{23}C_6$ size, $\mu m$					
	C(K)	Cr(K)	Fe(K)	Ni(K)	Mo(K)	ITB*, width	ITB, length	CTB**, width	CTB, length	Matrix, width	Matrix, length
10Q	4.95 $\pm 0.68$	37.37 $\pm 1.02$	37.03 $\pm 0.99$	15.32 $\pm 0.51$	1.79 $\pm 0.09$	34 $\pm 3$	278 $\pm 19$	60 $\pm 30$	260 $\pm 130$	50 $\pm 7$	483 $\pm 52$
10A	12.92 $\pm 0.75$	46.36 $\pm 0.98$	24.55 $\pm 0.89$	9.63 $\pm 0.49$	2.29 $\pm 0.12$	48 $\pm 6$	201 $\pm 58$	26 $\pm 4$	288 $\pm 48$	70 $\pm 4$	585 $\pm 173$
100A	6.13 $\pm 0.42$	50.20 $\pm 1.16$	26.11 $\pm 0.94$	11.32 $\pm 0.5$	2.27 $\pm 0.07$	61 $\pm 6$	351 $\pm 45$	65 $\pm 6$	1260 $\pm 470$	75 $\pm 8$	655 $\pm 136$

\* ITB: Incoherent Twin Boundary; \*\*CTB: Coherent Twin Boundary.

### 3.1.9 Results of Tensile Testing

Figure 16 displays the tensile curve for the 10Q, 10A, and 100A materials tested at room temperature. The tensile tests show similar properties for each of the static aging treatments, indicating that the differences observed in the microstructural analysis do not have a significant impact on the tensile properties. Future testing will need to be performed to check the creep and cyclic properties.

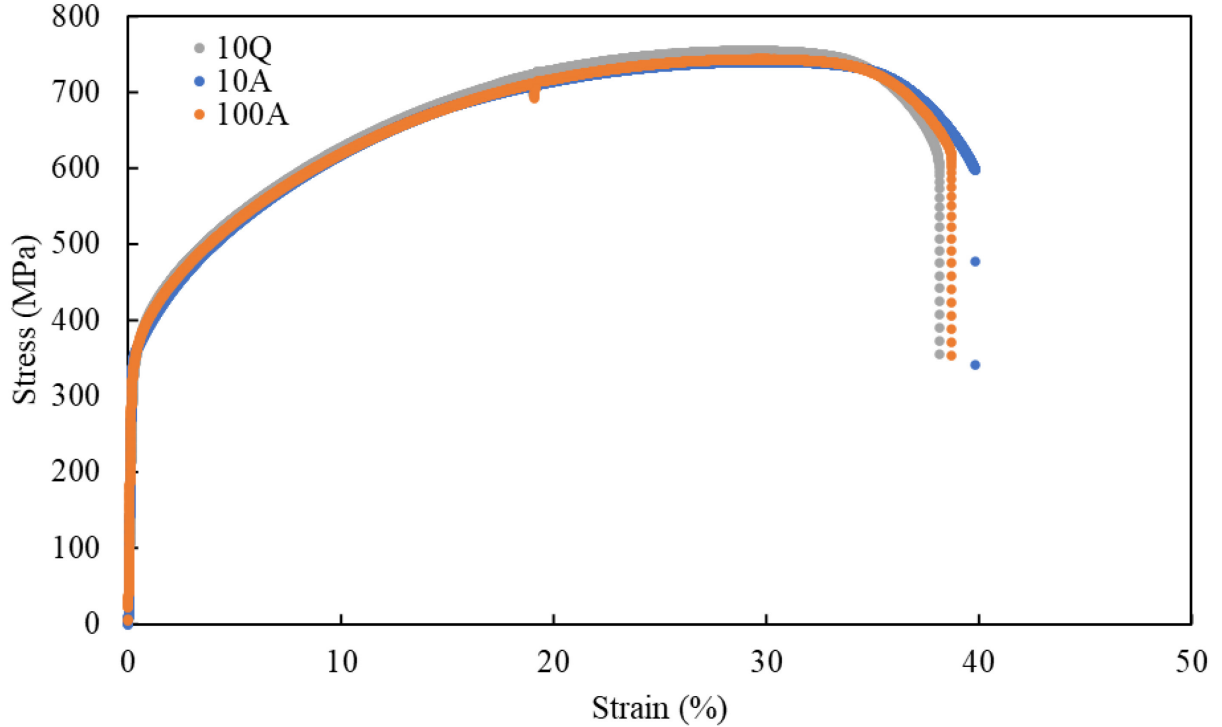


Figure 16. Engineering stress-strain curve of the 10Q, 10A and 100A samples.

### 3.2 Material Produced by ATI

TEM characterization was carried out on the hot-rolled plate solution-annealed at 1150°C minimum followed by water quench. Some preliminary TEM-EDS results showed that the existence of MX (likely NbC). More studies including low magnification LOM, TEM, and mechanical testing have been planned.

## 4. CONCLUSIONS

Detailed microstructural characterization was carried out on Alloy 709 plate from two different commercial heats. For the plate produced by Electralloy/G. O. Carlson, three static aging treatments were applied to the hot-rolled and 1150°C solution-annealed plates: (1) aged at 775°C for 10 hours and water quenched (10Q); (2) aged at 775°C for 10 hours and air cooled (10A); and (3) aged at 775°C for 100 hours and air cooled (100A). The following results were obtained:

- MX (Ni,Tb)(C,N) and  $M_{23}C_6$  (Cr,Mo)C precipitates were observed in all the static-aged samples.
- The grain size distribution in the 10Q and 100A samples were comparable, which means that grain structure was fairly stable when aging at 775°C for up to 100 hours in the Alloy 709. The 10A sample showed the smallest and the most uniform grain size distribution. It is, however, unlikely due to any change in grain structure resulting from the cooling process and is likely a result of the locations imaged, and grains characterized as this phenomenon was observed in only one sample. More samples would be needed to verify these results. If this observation is not repeatable, the difference between 10A and 10Q samples could be a result of microstructure inhomogeneity from earlier processing, rather than an effect of cooling.
- In comparison to the 10Q sample, there is no obvious difference in the composition and size of MX and  $M_{23}C_6$  precipitates in the 10A sample.

- Compared to the 10A sample, the 100A sample had a decreased number density of small precipitates, a higher ratio of small free precipitates without pinning dislocation, and a decreased dislocation density. In the 100A sample, the MX precipitates had a higher N, Nb and Ti composition. The  $M_{23}C_6$  precipitates on the incoherent and coherent boundaries of the 100A sample had a longer length, which may indicate some increase in  $M_{23}C_6$  size. Besides MX and  $M_{23}C_6$ , Si-enriched  $M_6X$  precipitate was also observed in the 100A sample after 100 hours static aging.
- The tensile tests showed similar properties for each of the static aging treatments, indicating that the differences observed in the microstructural analysis do not have a significant impact on the tensile properties.

For the plate produced by ATI, which was solution-annealed by isothermal holding at 1150 °C minimum and water quenched, some preliminary TEM-EDS results showed the existence of MX (likely NbC).

## **5. SUGGESTED FUTURE WORK**

Suggested future work for the plate produced by Electralloy/G. O. Carlson:

- Inclusion analysis.
- Quantitative study on Nb precipitates, how much Nb in precipitation/solution before and after solution annealing.
- Light optical microscopy on 1150°C solution-annealed samples at lower magnification, such as X50.
- Tensile, creep, and fatigue testing on 10A, 10Q, and 100A samples.
- Correlation between microstructure and mechanical properties.

Suggested future work for the plate produced by ATI:

- Inclusion analysis.
- Quantitative study on Nb precipitates, how much Nb in precipitation/solution before and after solution annealing.
- Microstructure characterization including light OM, EBSD, TEM, and EDS.
- Correlation between microstructure and mechanical properties.

## 6. REFERENCES

- [1] Natesan, K., X. Zhang, T.-L. Sham and H. Wang. Report on the Completion of the Procurement of the First Heat of Alloy 709, (No. ANL-ART-89), Argonne National Laboratory. Argonne, IL, 2017.
- [2] Sham, T.-L., and K. Natesan. 2017. Code Qualification Plan for an Advanced Austenite Stainless Steel, Alloy 709, for Sodium Fast Reactor Structural Application. International Conference on Fast Reactors and Related Fuel Cycles: Next Generation Nuclear for Sustainable Development (FR17), Yekaterinburg, Russia, IAEA-CN0245-74.
- [3] Rupp, R.E., and M.D. McMurtrey. 2020. Mechanical Properties of Aged A709, INL/EXT-20-59630-Rev000, Idaho National Laboratory.
- [4] Zhang, X., T.-L. Sham, and G.A. Young. 2019. Microstructural Characterization of Alloy 709 Plate Materials with Additional Heat Treatment Protocol. ANL-ART-170, Argonne National Laboratory. <https://doi.org/10.2172/1601459>.
- [5] Wright, R.N. 2020. Report Documenting Activity for Second Alloy 709 Commercial Heat. INL/EXT-20-59880-Rev000, Idaho National Laboratory.
- [6] ASTM Standard E8, Standard Test Methods for Tension Testing of Metallic Materials, West Conshohocken, PA: ASTM International, 2016.
- [7] Ding, R., J. Yan, H. Li, S. Yu, A. Rabiei and P. Bowen. Microstructural evolution of Alloy 709 during aging, *Materials Characterization*, 154 (2019) 400–423.
- [8] Irvine, K.J., F.B. Pickerling and T. Gladman. *J. Iron Steel Inst.*, 205 (1967) 161-182.
- [9] Sourmial, T., Precipitation in creep resistant austenitic stainless steels, *Mater. Sci. Technol.* 17(2001) 1–14.
- [10] Taylor, M., J. Ramirez, I. Charit, G.P. Potirniche, R. Stephens and M.V. Glazoff. Creep behavior of Alloy 709 at 700 °C. *Mater. Sci. & Eng A* 762 (2019) 138083.
- [11] Robinson, P.W., D.H. Jack, and R. Lula. New developments in stainless steel technology, American Society of Metals, Metals Park, OH, 1985, 71–76.
- [12] Sourmail, T., and H.K.D.H. Bhadeshia. Microstructural evolution in two variants of NF709 at 1023 and 1073 K, *Metall. Mater. Trans. A* 36 (2005) 23–34.